

Research Article

Experimental Characterization of a UWB Channel for Body Area Networks

Lingli Xia, Stephen Redfield, and Patrick Chiang

VLSI Research Group, Oregon State University, Corvallis, OR, 97331, USA

Correspondence should be addressed to Lingli Xia, xia@eecs.oregonstate.edu

Received 28 October 2010; Accepted 14 January 2011

Academic Editor: Philippe De Doncker

Copyright © 2011 Lingli Xia et al. This is an open access article distributed under the Creative Commons Attribution License, which permits unrestricted use, distribution, and reproduction in any medium, provided the original work is properly cited.

Ultrawideband (UWB) communication is a promising technology for wireless body area networks (BANs), especially for applications that require transmission of both low and high data rates with excellent energy efficiency. Therefore, understanding the unique UWB channel propagation characteristics around the human body is critical for a successful wireless system, especially for insuring the reliability of important vital sign data. Previous work has focused only on on-body channels, where both TX and RX antennas are located on the human body. In this paper, a 3–5 GHz UWB channel is measured and analyzed for human body wireless communications. Beyond the conventional on-body channel model, line-of-sight (LOS) and non-line-of-sight (NLOS) channel models are obtained using a TX antenna placed at various locations of the human body while the RX antenna is placed away from the human body. Measurement results indicate that the human body does not significantly degrade the impedance of a monopole omnidirectional antenna. The measured path loss and multipath analysis suggest that a LOS UWB channel is excellent for low-power, high-data-rate transmission, while NLOS and on-body channels need to be reconfigured to operate at a lower data rate due to high path loss.

1. Introduction

Recently, there has been an increased interest in using body area networks (BANs) for health monitoring [1–7]. A variety of physiological electrical signals from the human body can be continuously monitored wirelessly, including brain waves (EEG or electroencephalography), heart health (ECG or electrocardiography), and muscle response (EMG or electromyography). For a real-time vital sign monitoring system [1], as shown in Figure 1(a), a single (or multiple) wearable sensor node with a wireless transmitter is attached to a patient, while the receiver is attached to some nearby fixed location (i.e., wrist watch or ceiling). The sensor captures the real-time physiological signals, activating the transmitter that sends a low-data-rate signal to the receiver alerting a remote clinician through cellular or internet networks. Through this wireless body sensor network, disease prevention can be improved with this continuous real-time diagnosis, thus reducing the onset of degenerative diseases and healthcare costs.

A high data rate is not typically an important concern for body area networks, as sampling frequencies of front-end sensors is typically less than 1 kHz. For example, a heart reading using ECG requires at most 12 kbps or 12 b at 1 kHz. However, for body sensor applications that require tens or hundreds of sensing channels [2], a large bandwidth is necessary. One example is a handheld, wireless ultrasound module with hundreds of ADC channels, which need to send several megabits of data. Another example is in next-generation brain implants, which will require hundreds of cortical implant channels streamed wirelessly to a stationary receiver [3]. This large communication bandwidth will also be needed for an application where BAN data may firstly be stored locally on the sensor node, such as in a local data storage memory. Then when the patient goes to the hospital, the doctor can read these data through high-data-rate transmission and make a thorough diagnosis, as shown in Figure 1(b).

Traditional narrowband wireless protocols, such as MICS (medical implant communications service), Zigbee, ISM,

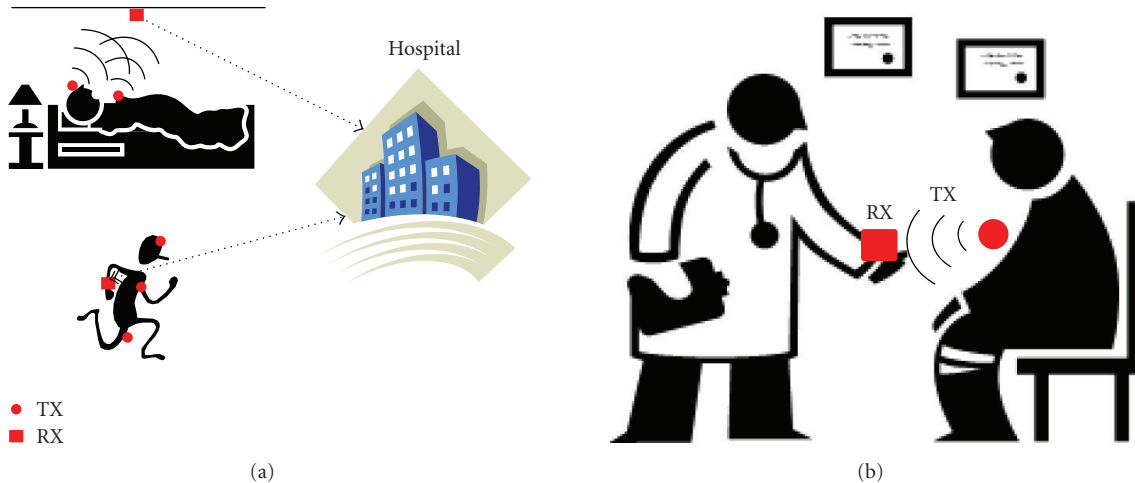


FIGURE 1: Body area networks for health monitoring: (a) low-data-rate transmission (b) high-data-rate transmission.

TABLE 1: LOS measurement results comparison.

		cc1101	cc1101	cc2500	This work
Frequency		433 MHz	868 MHz	2.4 GHz	3–5 GHz
Data rate		0.6~600 kbps	0.6~600 kbps	1.2~500 kbps	1~100 Mbps
Power consumption	TX	48 mW at 0 dBm	50.4 mW at 0 dBm	63.6 mW at 0 dBm	4.44 mW at -41.3 dBm/MHz
	RX	45~51.3 mW	43.8~50.7 mW	39.9~58.8 mW	13.2 mW
BER at RSSI		0.2% at -51 dBm	0.1% at -63 dBm	$<0.1\%$ at -64 dBm	1% at -50 dBm
Antenna size		Large	Medium	Small	Medium

and Bluetooth standards [4, 5], suffer from large power consumption and low data rate, as listed in Table 1. Unlike these traditional narrowband systems, ultrawideband (UWB) wireless sensors operate with a large bandwidth (3.1–10.6 GHz) and a low maximum transmission spectral density (-41.3 dBm/MHz). According to Shannon-Hartley theorem, with an ultra-wide bandwidth, high data rate can be achieved with low transmitted power in UWB.

Power consumption is also a critical requirement for body area networks, as patients may choose to not adopt such body sensors if the sensors need to be recharged frequently. Furthermore, low power consumption results in a smaller battery size, significantly reducing sensor cost and form factor. Consider a 3–5 GHz impulse radio UWB (IR-UWB) transceiver that we developed, shown in Figure 2. An IR-UWB transceiver does not require DAC, PLL, or PA. Here the transmitter consists of only a pulse generator, an output buffer, and a power control block [8]. A configurable data rate can be easily realized by changing the pulse repetition rate. The duty-cycled characteristic of the transmitted signals is employed to turn off the output buffer during pulses intervals, further lowering the power consumption. Measurement results show that the power consumption of the transmitter is only $400 \mu\text{W}$ and 4.44 mW with data rates of 1 Mbps and 100 Mbps, respectively. Meanwhile, the receiver employs a noncoherent architecture, consuming 13.2 mW with a data rate of 100 Mbps. Table 1 summarizes the measurement

results of the proposed UWB transceiver and two off-the-shelf chips (TI cc1101 and TI cc2500).

Knowledge of the channel model for UWB transmission is critical for any robust transceiver system. Moreover, body area networks exhibit unique radio propagation characteristics combining line of sight, creeping wave, multiple reflections from surrounding environments, and diffraction around the human body. Ever since the FCC released unlicensed spectrum for UWB, several previous works on UWB channel modeling have been published. Molisch et al. [9] developed an IEEE 802.15.4a channel model for various low-rate UWB applications, where the body area network channel model is analyzed using a finite difference time-domain (FDTD) simulator with antennas moving around the human body. Wang et al. [10] also used FDTD method to simulate various body postures based on a realistic human body model. Unfortunately, these numerical approaches neglect considerations of the surrounding environments, which are the main sources of multipath.

Furthermore, the previous investigations only considered data transmission with both TX and RX antennas on the human body, which is not the dominant usage model. In this paper, we present a complete UWB channel model that not only considers on-body UWB propagation but also extends to include LOS and NLOS channel measurement, using a TX antenna placed on the human body and a separate RX antenna located externally. Section 2 introduces

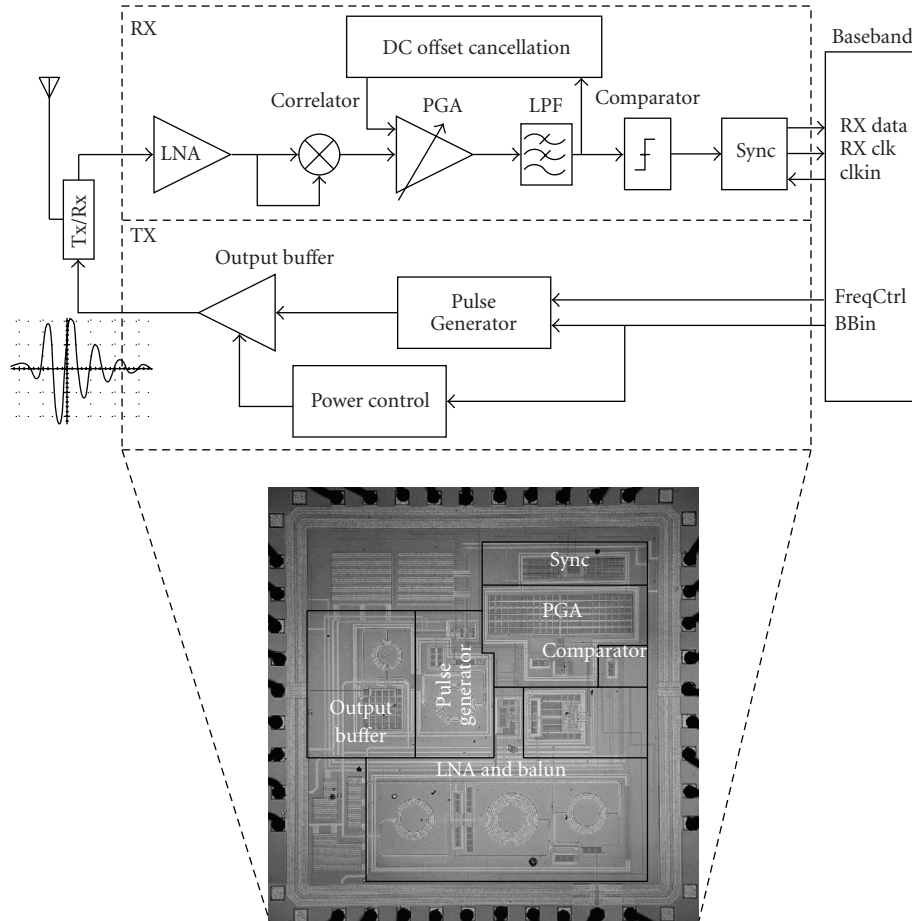


FIGURE 2: Impulse radio UWB transceiver architecture.

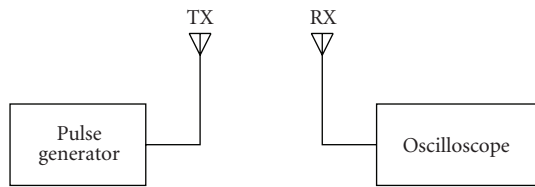


FIGURE 3: Time-domain measurement setup.

the measurement setup of this work, Section 3 discusses the measurement results and provides a thorough analysis on different channels, and Section 4 draws a conclusion.

2. Measurement Setup

In this work, the UWB radio channel measurement is performed in an EM-shielded lab with a height of 3.5 m. The lab resembles an ordinary room with concrete walls, ceiling, desks, and chairs. When the door is closed, the lab is protected from EM interferences by metallic panels behind the walls and ceiling. This enables accurate estimation of local multipath propagation, with sufficient interference rejection.

Channel measurements can be conducted in the time domain based on impulse transmission or the frequency domain using a frequency sweep technique [11]. In the former setup, as shown in Figure 3, UWB impulses are generated by a pulse generator and transmitted through an antenna. After wireless propagation, the impulses are received by an RX antenna and sampled by an oscilloscope, where subsequent time-domain algorithms are performed in order to calculate the path loss and power delay profile (PDP) [12]. In the latter setup, a vector network analyzer (VNA) is employed that captures the frequency response of the UWB channel as a S21 parameter, followed by generation of a channel impulse response (CIR) in the time domain, obtained by performing an inverse Fourier transform (IFT). In this work, a VNA-based measurement setup is employed. The VNA (HP 8520ES) is used to capture 1061 data points between 3 and 5 GHz, providing a frequency-domain resolution of 1.25 MHz. As shown in Figure 4, the following three conditions are measured.

(a) *Line-of-Sight*. There is no object obstructing the TX and RX antennas. The TX antenna is placed on the head, chest, and left thigh of the human body while the RX antenna is placed at the same height off the human body.

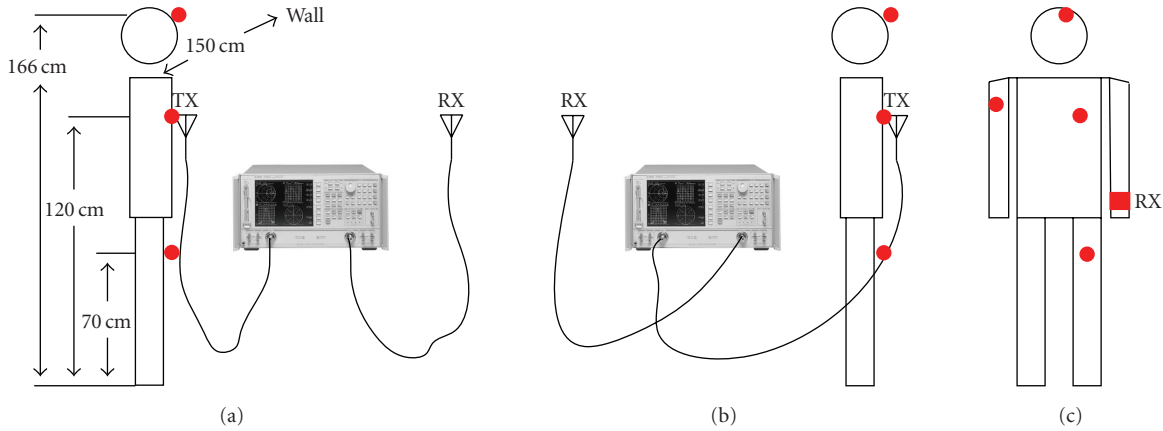


FIGURE 4: Frequency-domain measurement setup: (a) line-of-sight; (b) non-line-of-sight; (c) on-body.

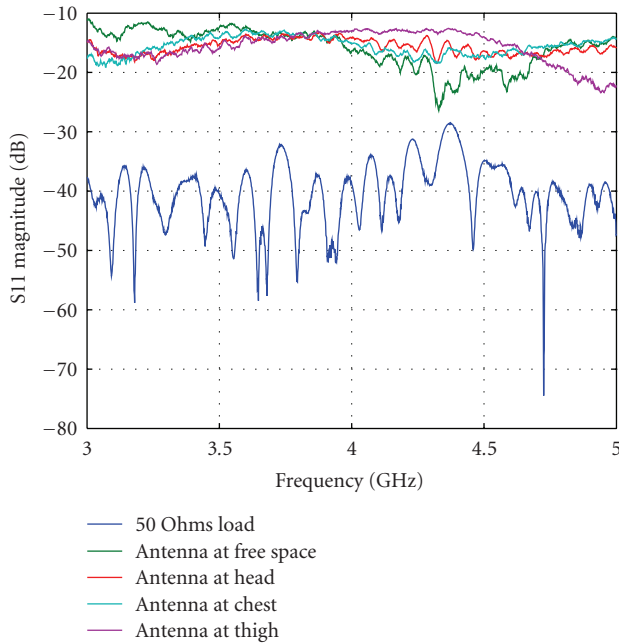


FIGURE 5: Measured return loss of the antenna.

(b) *Non-Line-of-Sight*. The transmission between the TX and RX antennas is interrupted by the human body.

(c) *On-Body*. Both TX and RX antennas are placed on the human body. The RX antenna is worn on the left wrist while the TX antenna is able to freely move around.

The antennas used in the measurement are monopole omnidirectional antennas from 3–5 GHz, manufactured by Fractus Corporation. Calibration is performed to eliminate the loss of the cables and connectors. The measured antenna return loss (on and off the human body) is shown in Figure 5. As observed, the antenna shows excellent impedance matching on and off the human body with the return loss (S11) below -10 dB across the entire 3–5 GHz. Note that the antenna return loss near the human body is different

from free space, as the antenna characteristic impedance is changed by the high dielectric permittivity and conductivity of the human body tissues [13].

3. UWB Radio Channel Measurement Results

3.1. Propagation Path Loss

3.1.1. *Frequency Dependence*. Path loss is the reduction in power as the transmitted signal propagates through space. According to Friis's transmission equation, the path loss is

$$L = \left(\frac{4\pi f}{c} \right) d^n, \quad (1)$$

where c is the speed of light, d is the distance between the TX and RX antennas, and n is the path loss exponent, whose value is normally 2 for propagation in free space. While the frequency dependence of the path loss is usually ignored in narrow band systems, it cannot be ignored in UWB systems due to the large bandwidth. Figure 6(a) shows the measured S21 of the channel when the distance d is 3 cm (the calculated free space frequency-dependent loss is also plotted as a comparison). As observed, the frequency response of the LOS channel is different from free space transmission because of the absorption and reflection off of the human tissue, as well as the surrounding environments which are also frequency dependent. As the transmission distance extends to 1 m, the multipath signals increase, such that the LOS path loss is less than the free space path loss, as shown in Figure 6(b). Figure 6(c) shows that for the measured S21 of a 1 m NLOS channel, the path loss is greatly worsened, as the UWB signal is unable to transmit through the human body. In this NLOS situation, the measured received power comes predominantly from the reflections of the surrounding environments and the diffracted signal from the human body. Finally, on-body channel characteristics are also measured, as in Figure 6(d), showing that the left wrist to right thigh channel exhibits larger path loss than left wrist to left thigh channel, as the transmission distance is increased.

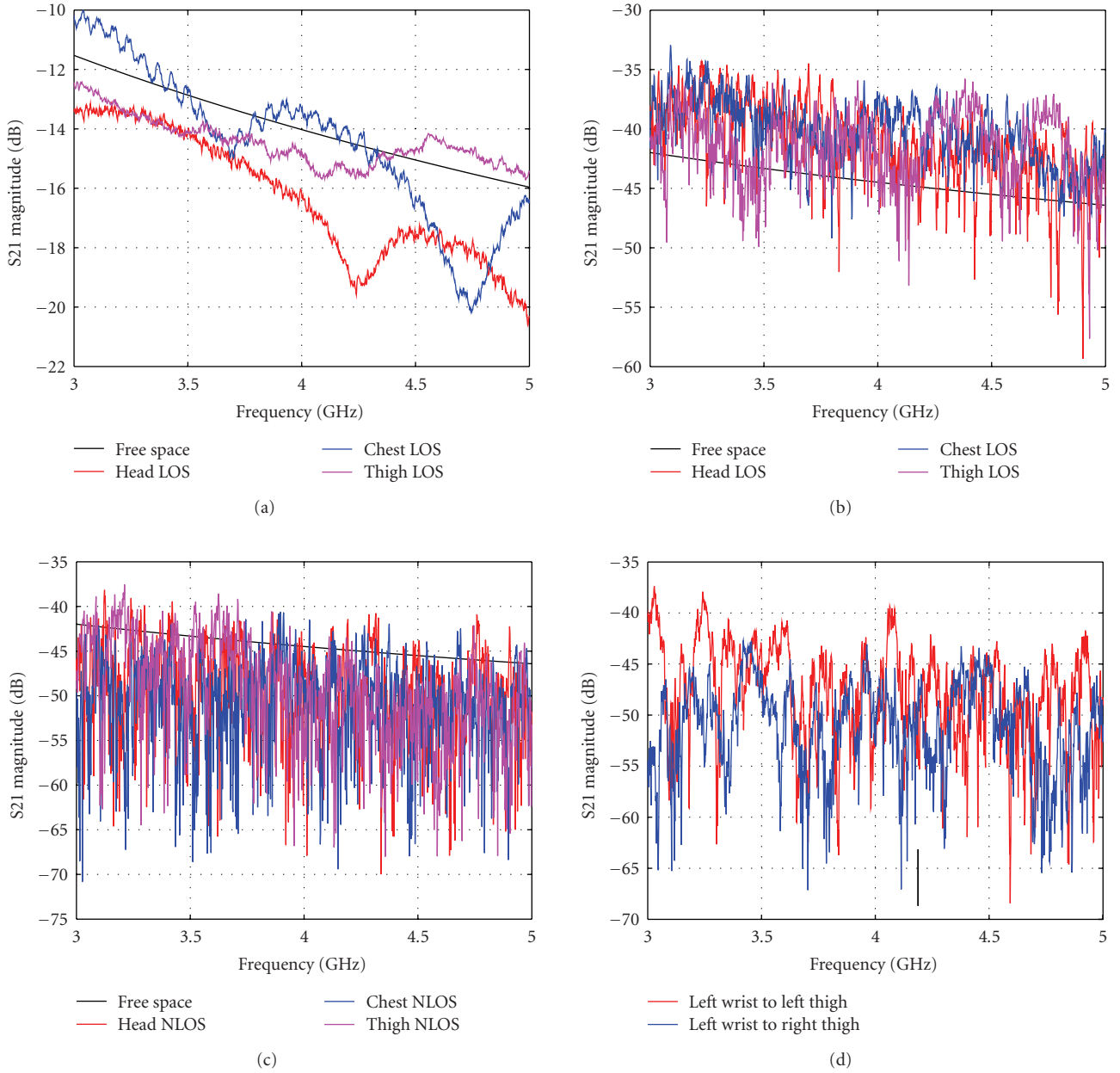


FIGURE 6: Frequency-dependent characteristics of UWB channel: (a) LOS at 3 cm; (b) LOS at 1 m; (c) NLOS at 1 m; (d) on-body channel.

3.1.2. *Distance Dependence.* Path loss (dB) is typically expressed as

$$PL(d) = PL(d_0) + 10 \cdot n \cdot \log\left(\frac{d}{d_0}\right) + \chi, \quad (2)$$

where d_0 is a reference distance and χ is a random variable with a zero-mean Gaussian distribution. In order to eliminate the impact of frequency, the distance-dependent path loss is obtained by averaging the measured frequency response [15]:

$$PL(d) = 10 \log\left(\frac{1}{N} \sum_{i=1}^N |H(f_i, d)|^2\right), \quad (3)$$

where N is the number of the swept frequency points and $H(f_i, d)$ is the frequency response S21 of the channel measured by a VNA. In Figure 7(a), a linear regression fit is performed in order to calculate the path loss exponent n in a LOS channel measurement. The far-field path loss exponent in this work is different from the previous works [9, 10, 14, 16, 17], because only the TX antenna is put on the human body and the reflective environments are also considered in this LOS measurement setup. Table 2 lists the measured results and the comparison with previous works. The standard deviation of the normal distribution χ is also calculated in order to improve the accuracy of (2), as shown in Figure 7(b). Figure 7(c) shows the distance-dependent path loss in an NLOS measurement. The NLOS channel path

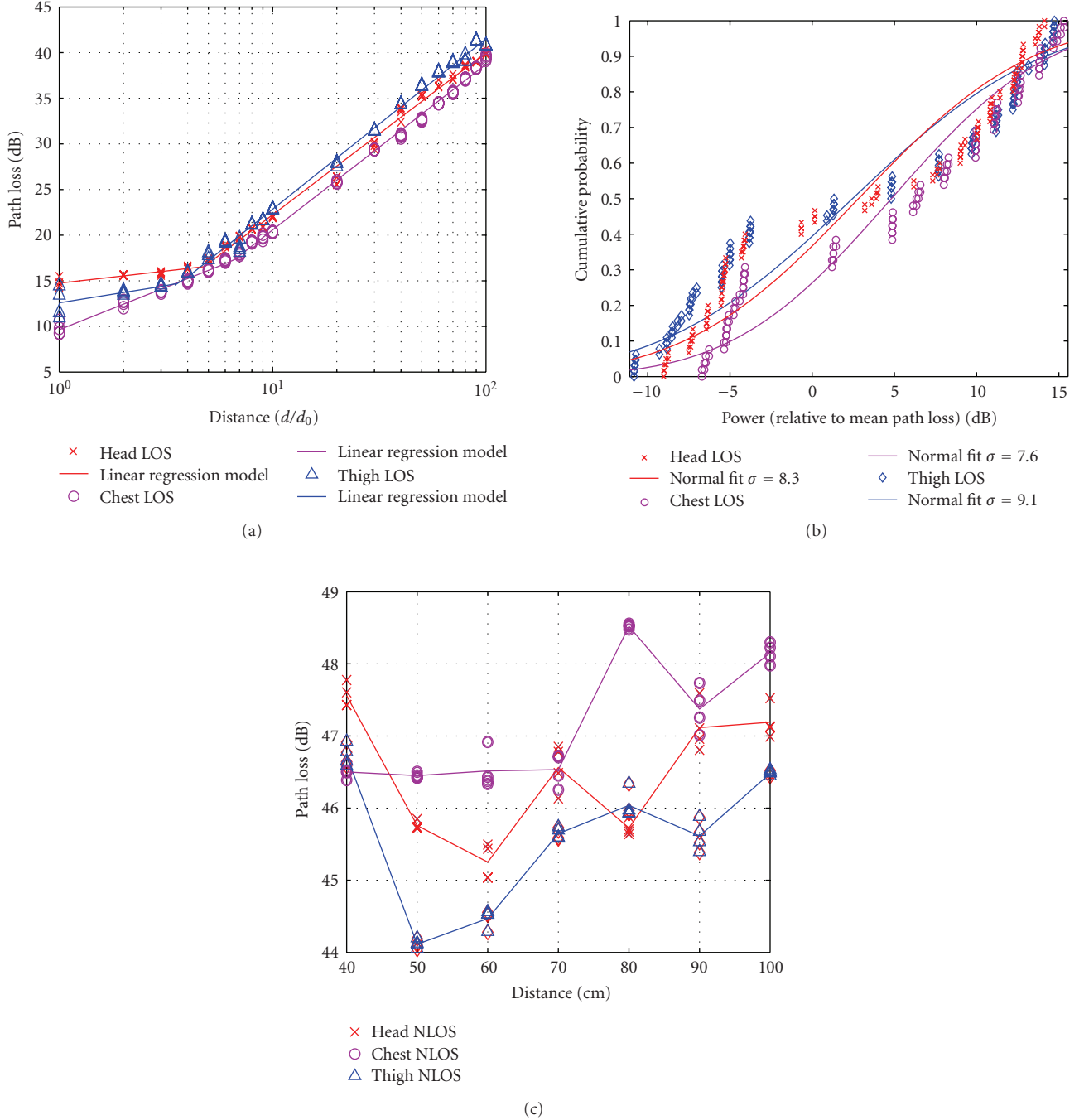


FIGURE 7: Distance-dependent path loss: (a) LOS path loss; (b) cumulative probability of far-field LOS path loss; (c) NLOS path loss.

loss does not show a linear-logarithmic characteristic as the LOS channel; instead, the path loss changes slightly as the distance extends. The reason is that when the human body interrupts with the transmission channel, the area of the human body that interrupts the signal becomes small relative to the distance between the antennas, such that the diffracted signal becomes stronger [18]. Note that the path loss of the on-body channel is much larger than the LOS channel and comparable with that of the NLOS channel, as can be seen in Table 3.

3.2. RMS Delay Spread. The power delay profile shows the received signal power as a function of time delay, giving an intuitive inspection of the multipath channel. Power delay profile can be obtained by implementing an IFT on the measured data:

$$\text{PDP} = 20 \log |h(t)| = 20 \log \left| \sum_{k=0}^{N-1} \Delta f \cdot H(k \cdot \Delta f) \cdot e^{j2\pi kn/N} \right|, \quad (4)$$

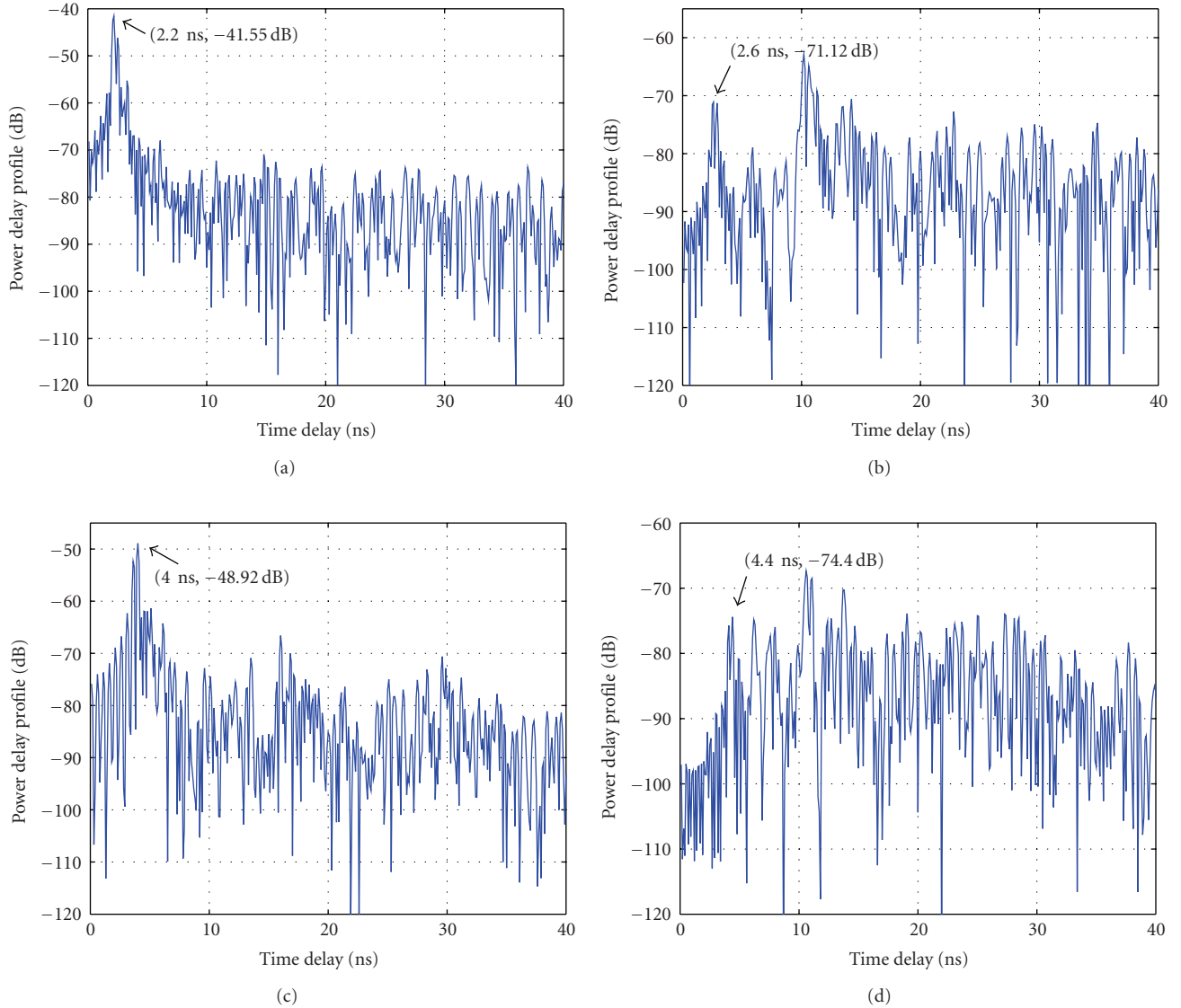


FIGURE 8: Power delay profile when placing TX antenna on the chest: (a) LOS at 50 cm; (b) NLOS at 50 cm; (c) LOS at 1 m; (d) NLOS at 1 m.

TABLE 2: Comparison of parameter values for distance-dependent path loss model.

	Position	Near-field n	Far-field n	Far-field σ	Far-field fit
This work	Head	0.27	1.78	8.3	Normal
	Chest	0.93	1.82	7.6	
	Muscle	0.37	1.87	9.1	
[9]	Torso front	—	1.08	4.7	Lognormal
	Torso side	—	1.08	6.3	
	Torso back	—	1.08	6.3	
[14] (multiantenna)	Torso front	—	1.26	3.87 (tap 1)	Lognormal
	Torso back	—	1.26	5.64 (tap 1)	

where $h(t)$ is the UWB channel impulse response (CIR) in the time domain and $H(f)$ is the measured UWB channel frequency response. Hermitian signal processing is employed to obtain a real-valued CIR by zero padding the lowest frequency down to DC, taking the conjugate of the signal,

and reflecting it to the negative frequency [19]. Figure 8 shows the power delay profile of both LOS and NLOS channels after placing the TX antenna on the chest. As observed, the received power is greatly reduced due to the LOS interruption caused by the human body within

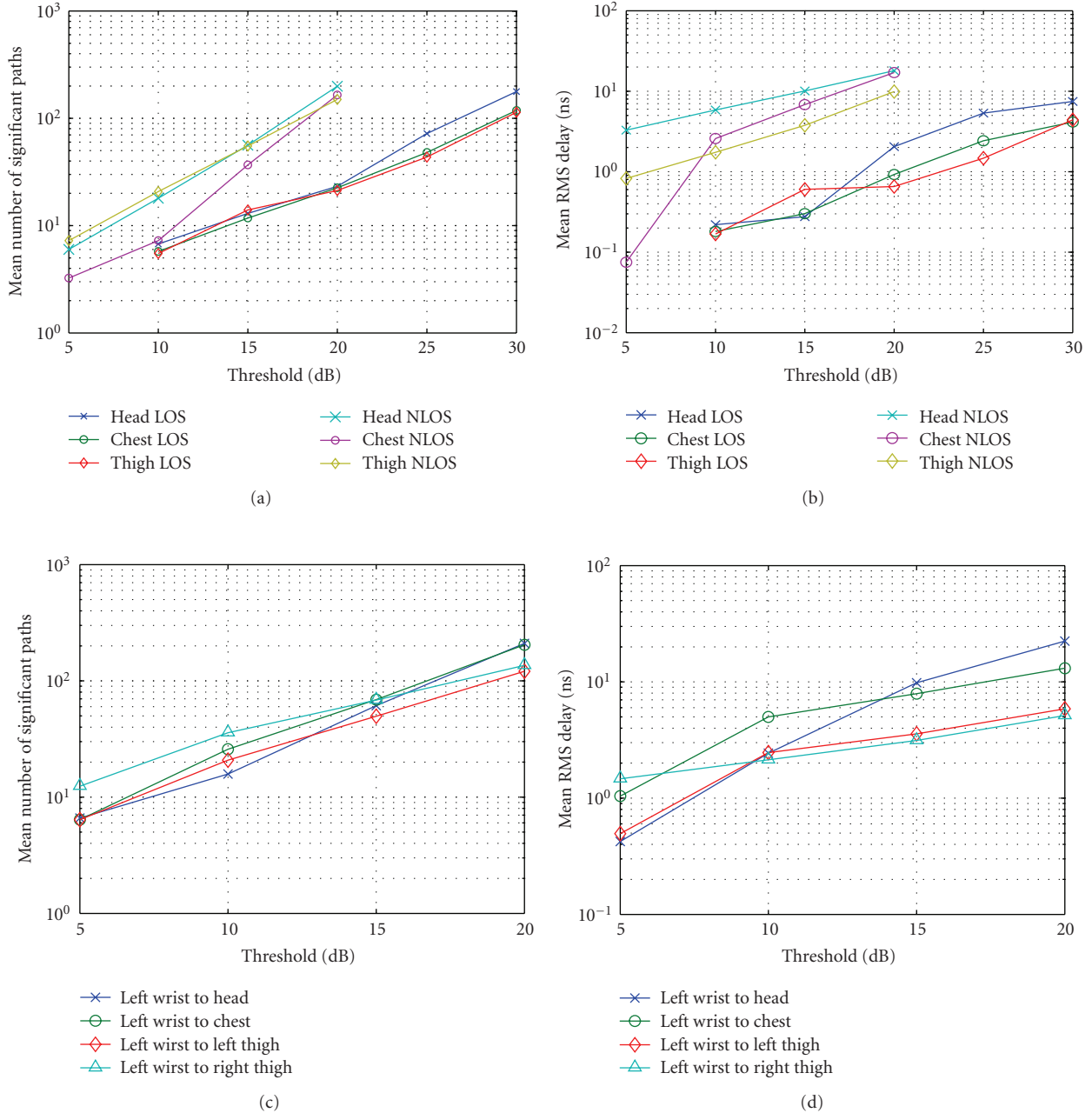


FIGURE 9: Mean RMS delay spread versus threshold: (a) multipath number at 1 m; (b) RMS delay time at 1 m; (c) multipath number at on-body channel; (d) RMS delay time at on-body channel.

TABLE 3: Path loss of on-body channels.

Left wrist to distance (cm)	Head	Chest	Left thigh	Right thigh
85	85	45	20	40
path loss (dB)	51.4	49.4	45.5	49.4

the NLOS channel. However, because of the diffraction around the human body, the RX antenna still captures some detectable power at delay times of 2.6 ns and 4.4 ns in the NLOS channel at distances of 50 cm and 1 m, respectively.

Another important phenomenon is that in a LOS channel, the received direct path power reduces by 7.4 dB when the distance extends from 50 cm to 1 m. In an NLOS channel, the received diffracted power reduces by only 3.3 dB. This manifestation occurs because the area of the interruption caused by the human body becomes relatively smaller as the distance is increased, coinciding with the results of Figure 7(c).

Delay spread is a measure of the multipath density within a wireless channel and an important characteristic when comparing between different channels. Mean delay

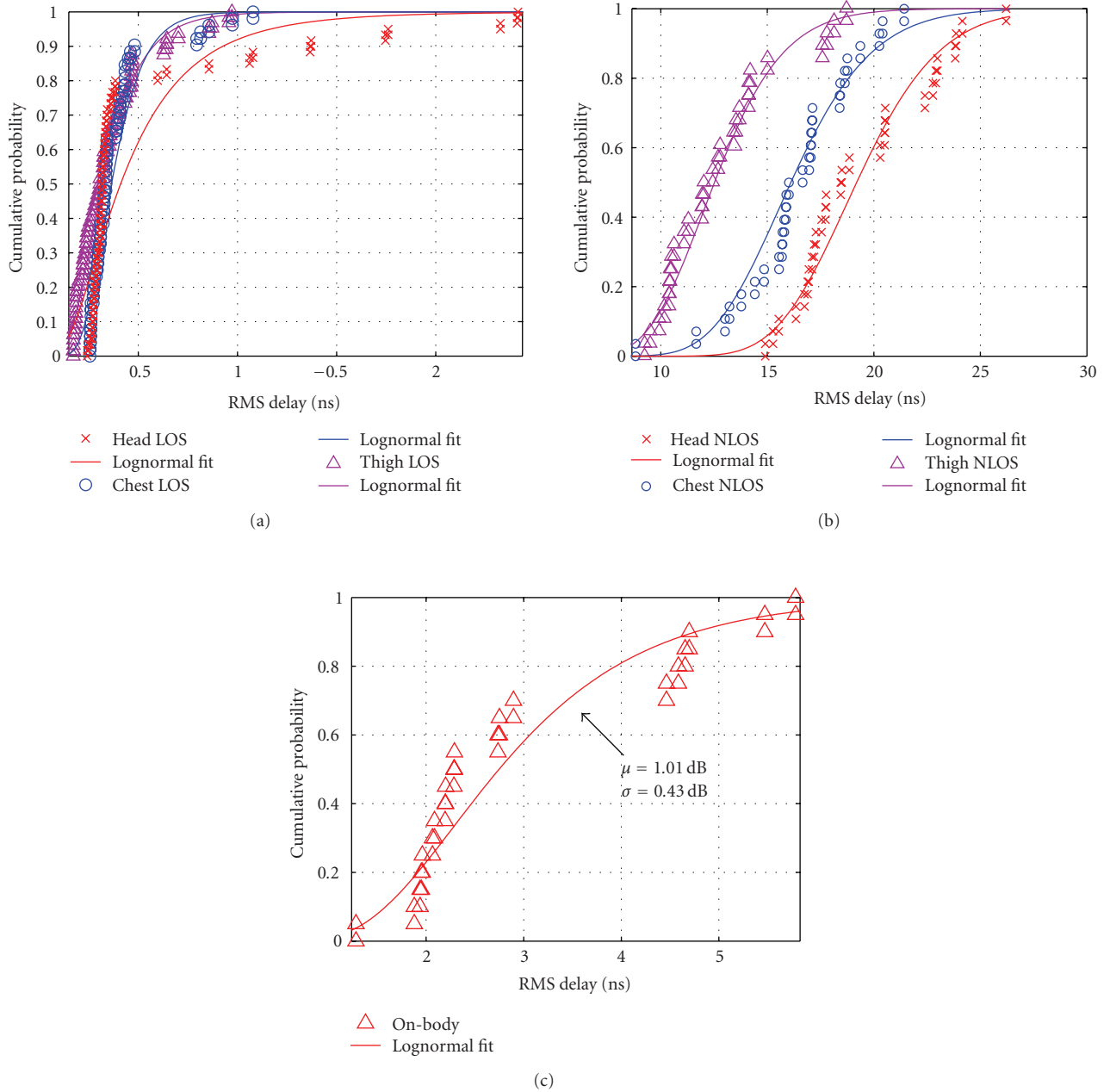


FIGURE 10: Cumulative probability of the RMS delay spread fitted to lognormal delay with 20 dB threshold (a) LOS (b) NLOS (c) on-body.

spread, RMS delay spread, and maximum delay spread are three multipath channel parameters that can be determined from the power delay profile [20]. Mean delay spread is the average delay weighted by power:

$$\bar{\tau} = \frac{\sum_k a_k^2 \tau_k}{\sum_k a_k^2} = \frac{\sum_k P(\tau_k) \tau_k}{\sum_k P(\tau_k)}, \quad (5)$$

where a_k is the amplitude of the received signal and τ_k is the delay relative to the first detectable signal at the receiver.

RMS delay spread is the energy-weighted standard deviation of the signal delays:

$$\tau_{\text{rms}} = \sqrt{\tau^2 - (\bar{\tau})^2} = \sqrt{\frac{\sum_k a_k^2 \tau_k^2}{\sum_k a_k^2} - \left(\frac{\sum_k a_k^2 \tau_k}{\sum_k a_k^2} \right)^2}. \quad (6)$$

Maximum delay spread is the time difference between the arrival of the first and last significant signals. Among these, RMS delay spread is the most commonly used parameter because of its effect on the bit error rate and maximum data rate. Figure 9 shows the relationship between RMS

TABLE 4: Lognormal fitting model of the RMS delay spread.

	Head		Chest		Thigh	
	μ_{dB}	σ_{dB}	μ_{dB}	σ_{dB}	μ_{dB}	σ_{dB}
LOS						
Threshold (dB)						
20	-0.89	0.63	-1.01	0.35	-1.15	0.46
30	0.15	1.08	-0.01	0.89	-0.13	1.03
NLOS						
Threshold (dB)						
10	1.79	0.33	-0.40	1.24	0.89	0.38
20	2.95	0.16	2.78	0.18	2.53	0.20

delay spread and the minimum detectable power threshold for a 1 m transmission distance. As observed, the number of significant paths increases exponentially with the power threshold in LOS, NLOS, and on-body channels. However RMS delay time does not show the same characteristic, as the contribution of newly detected paths declines as the threshold increases [21]. An NLOS channel suffers more severe multipath effect and larger RMS delay spread than a LOS channel because of the interruption of the human body. Figures 9(c) and 9(d) show on-body channel measurement results with both TX and RX antennas placed on the human body. The multipath number and RMS delay time in a left wrist to left thigh channel are less than those in a left wrist to right thigh channel in low threshold detection because of the shorter transmission distance. However, the RMS delay spread is less significant as the threshold increases. This phenomenon is likely because both of these two channels share the same surrounding environments, for example, the same distance away from the floor. The cumulative probability of the RMS delay spread with a threshold of 20 dB is shown in Figure 10. Table 4 summarizes the average value and the standard deviation (μ and σ) of the lognormal fitting model.

4. Conclusion

Ultrawideband communication is a promising technology for next generation body sensor networks due to its potential for both low power and large bandwidth, currently unavailable using conventional narrowband systems. In this paper, both line-of-sight (LOS) and non-line-of-sight (NLOS) channels with various TX and RX antennas placed near the human are characterized. The frequency- and distance-dependent characteristics of a UWB channel are analyzed in this paper, where an NLOS channel is shown to have larger path loss than a LOS channel due to the physical interruption of the human body. Moreover, the path loss of an on-body channel is comparable with an NLOS channel. RMS delay spread is presented which provides an intuitive inspection of the multipath richness of a variety of channels. According to the experimental and analytical results, UWB systems with high data rate will require LOS channel characteristics. For sensor network application where only low-data-rate transmission is needed, NLOS and on-body channels can exhibit good performance using UWB.

References

- [1] J. Pan, "Medical applications of ultra-wideband (UWB)," <http://www1.cse.wustl.edu/~jain/cse574-08/ftp/uwb/index.html>.
- [2] M. Milanese, N. Martini, N. Vanello et al., "Multichannel techniques for motion artifacts removal from electrocardiographic signals," in *Proceedings of the 28th Annual International Conference of the IEEE Engineering in Medicine and Biology Society (EMBS '06)*, pp. 3391–3394, September 2006.
- [3] H. Miranda, V. Gilja, C. A. Chestek, K. V. Shenoy, and T. H. Meng, "HermesD: a high-rate long-range wireless transmission system for simultaneous multichannel neural recording applications," *IEEE Transactions on Biomedical Circuits and Systems*, vol. 4, no. 3, pp. 181–191, 2010.
- [4] B. Yu, L. Yang, and C.-C. Chong, "ECG monitoring over bluetooth: data compression and transmission," in *Proceedings of IEEE Wireless Communications and Networking Conference (WCNC '10)*, 2010.
- [5] M. R. Yuce, S. W. P. Ng, N. L. Myo, C. K. Lee, J. Y. Khan, and W. Liu, "A MICS band wireless body sensor network," in *Proceedings of IEEE Wireless Communications and Networking Conference (WCNC '07)*, pp. 2475–2480, 2007.
- [6] A. Khaleghi, R. Chávez-Santiago, and I. Balasingham, "Ultra-wideband pulse-based data communications for medical implants," *IET Communications*, vol. 4, no. 15, pp. 1889–1897, 2010.
- [7] T. Nakagawa, G. Ono, R. Fujiwara, T. Norimatsu, T. Terada, and M. Miyazaki, "Fully integrated UWB-IR CMOS transceiver for wireless body area networks," in *Proceedings of IEEE International Conference on Ultra-Wideband (ICUWB '09)*, pp. 768–772, September 2009.
- [8] L. Xia, Y. Huang, and Z. Hong, "Low power amplitude and spectrum tunable IR-UWB transmitter," *Electronics Letters*, vol. 44, no. 20, pp. 1200–1201, 2008.
- [9] A. F. Molisch et al., "IEEE 802.15.4a channel model—final report," IEEE 802.15.04-0662-01-004a, November 2004.
- [10] Q. Wang, T. Tayamachi, I. Kimura, and J. Wang, "An on-body channel model for UWB body area communications for various postures," *IEEE Transactions on Antennas and Propagation*, vol. 57, no. 4, pp. 991–998, 2009.
- [11] M. Hamalainen, T. Patsi, and V. Hovinen, "Ultra wideband indoor radio channel measurements," <http://www.ee.oulu.fi/>.
- [12] Y. Chen, J. Teo, J. Lai et al., "Cooperative communications in ultra-wideband wireless body area networks: channel modeling and system diversity analysis," *IEEE Journal on Selected Areas in Communications*, vol. 27, no. 1, Article ID 4740881, pp. 5–16, 2009.
- [13] A. Khaleghi and I. Balasingham, "Non-line-of-sight on-body ultra wideband (1–6 GHz) channel characterisation using different antenna polarisations," *IET Microwaves, Antennas and Propagation*, vol. 3, no. 7, pp. 1019–1027, 2009.
- [14] S. Van Roy, C. Oestges, F. Horlin, and P. De Doncker, "A comprehensive channel model for UWB multisensor multi-antenna body area networks," *IEEE Transactions on Antennas and Propagation*, vol. 58, no. 1, pp. 163–170, 2010.
- [15] J. A. Dabin, N. Ni, A. M. Haimovich, E. Niver, and H. Grebel, "The effects of antenna directivity on path loss and multipath propagation in UWB indoor wireless channels," in *Proceedings of IEEE Conference on Ultra Wideband Systems and Technologies*, pp. 305–309, November 2003.
- [16] A. Sani, A. Alomainy, G. Palikaras et al., "Experimental characterization of UWB on-body radio channel in indoor

- environment considering different antennas,” *IEEE Transactions on Antennas and Propagation*, vol. 58, no. 1, pp. 238–241, 2010.
- [17] A. Fort, J. Ryckaert, C. Desset, P. De Doncker, P. Wambacq, and L. Van Biesen, “Ultra-wideband channel model for communication around the human body,” *IEEE Journal on Selected Areas in Communications*, vol. 24, no. 4, pp. 927–933, 2006.
- [18] K. Watanabe, S. Hari, K. Ohno, and T. Ikegami, “Experiments on shadow effects of body and effective paths for UWB transmission in BAN,” in *Proceedings of the International Symposium on Communications and Information Technologies (ISCIT '08)*, pp. 232–237, October 2008.
- [19] I. Oppermann, M. Hamalainen, and J. Linatti, *UWB Theory and Applications*, John Wiley & Sons, 2004.
- [20] J. J. W. Siemons, *Measurement Based Indoor Radio Channel Model*, Koninklijke Philips Electronics, 2000.
- [21] J.-Y. Lee, “UWB channel modeling in roadway and indoor parking environments,” *IEEE Transactions on Vehicular Technology*, vol. 59, no. 7, pp. 3171–3180, 2010.



Preliminary call for papers

The 2011 European Signal Processing Conference (EUSIPCO-2011) is the nineteenth in a series of conferences promoted by the European Association for Signal Processing (EURASIP, www.urasip.org). This year edition will take place in Barcelona, capital city of Catalonia (Spain), and will be jointly organized by the Centre Tecnològic de Telecomunicacions de Catalunya (CTTC) and the Universitat Politècnica de Catalunya (UPC).

EUSIPCO-2011 will focus on key aspects of signal processing theory and applications as listed below. Acceptance of submissions will be based on quality, relevance and originality. Accepted papers will be published in the EUSIPCO proceedings and presented during the conference. Paper submissions, proposals for tutorials and proposals for special sessions are invited in, but not limited to, the following areas of interest.

Areas of Interest

- Audio and electro-acoustics.
- Design, implementation, and applications of signal processing systems.
- Multimedia signal processing and coding.
- Image and multidimensional signal processing.
- Signal detection and estimation.
- Sensor array and multi-channel signal processing.
- Sensor fusion in networked systems.
- Signal processing for communications.
- Medical imaging and image analysis.
- Non-stationary, non-linear and non-Gaussian signal processing.

Submissions

Procedures to submit a paper and proposals for special sessions and tutorials will be detailed at www.eusipco2011.org. Submitted papers must be camera-ready, no more than 5 pages long, and conforming to the standard specified on the EUSIPCO 2011 web site. First authors who are registered students can participate in the best student paper competition.

Important Deadlines:



Proposals for special sessions	15 Dec 2010
Proposals for tutorials	18 Feb 2011
Electronic submission of full papers	21 Feb 2011
Notification of acceptance	23 May 2011
Submission of camera-ready papers	6 Jun 2011

Webpage: www.eusipco2011.org

Organizing Committee

Honorary Chair

Miguel A. Lagunas (CTTC)

General Chair

Ana I. Pérez-Neira (UPC)

General Vice-Chair

Carles Antón-Haro (CTTC)

Technical Program Chair

Xavier Mestre (CTTC)

Technical Program Co-Chairs

Javier Hernando (UPC)

Montserrat Pardàs (UPC)

Plenary Talks

Ferran Marqués (UPC)

Yonina Eldar (Technion)

Special Sessions

Ignacio Santamaría (Universidad de Cantabria)

Mats Bengtsson (KTH)

Finances

Montserrat Najar (UPC)

Tutorials

Daniel P. Palomar

(Hong Kong UST)

Beatrice Pesquet-Popescu (ENST)

Publicity

Stephan Pfletschinger (CTTC)

Mònica Navarro (CTTC)

Publications

Antonio Pascual (UPC)

Carles Fernández (CTTC)

Industrial Liaison & Exhibits

Angeliki Alexiou

(University of Piraeus)

Albert Sitjà (CTTC)

International Liaison

Ju Liu (Shandong University-China)

Jinhong Yuan (UNSW-Australia)

Tamas Sziranyi (SZTAKI -Hungary)

Rich Stern (CMU-USA)

Ricardo L. de Queiroz (UNB-Brazil)

